This article has been accepted for publication in a future issue of this journal, but has not been fully edited. Content may change prior to final publication. Citation information: DOI 10.1109/TIP.2016.2523345, IEEE Transactions on Image Processing

Framelet based Sparse Unmixing of Hyperspectral Images

Guixu Zhang, Yingying Xu, and Faming Fang*

***Abstract*—Spectral unmixing aims at estimating the proportions (abundances) of pure spectrums (endmembers) in each mixed pixel of hyperspectral data. Recently, semi-supervised approach which takes the spectral library as prior knowledge has been attracting much attention in unmixing. In this paper, we propose a new semi-supervised unmixing model termed framelet based sparse unmixing (FSU) which promotes the abundance sparsity in framelet domain, and discriminates the approximation and detail components of hyperspectral data after framelet decomposition. Due to the advantages of the framelet representations, e.g., images have good sparse approximations in framelet domain, and most of the additive noises are included in the detail coefficients, the FSU model has a better antinoise capability, and accordingly leads to more desirable unmixing performance. The existence and uniqueness of the minimizer of the FSU model is then discussed, and the split Bregman algorithm as well as its convergence property are presented to obtain the minimal solution. Experimental results on both simulated data and real data demonstrate that the FSU model generally performs better than the compared methods.**

***Index Terms*—Hyperspectral image, sparse unmixing, framelet, abundance estimation, split Bregman.**

I. Introduction

Hyperspectral remote sensing is a type of earth observation technology which can acquire hyperspectral images. The hyperspectral image is a data cube in high dimension that can reflect both spatial and spectral information of ground objects and is characterized by high spectral resolution and relatively low spatial resolution. Hyperspectral remote sensing has attracted increasing attention for its widespread applications, such as mineral exploration [1], [2], terrain classification, environmental monitoring, military surveillance [3], [4], etc.

Since the spatial resolution of the hyperspectral image is generally low, a single pixel may contain several different material substances (named *endmembers*), each possessing a different hyperspectral signature [5], [6]. In this case, the measured spectrum of each pixel is a mixture of several endmember spectra, weighted by their fractions, called *abundances* [7], [8]. The existence of mixed pixels decreases the precise of many applications, thus becoming one of the most important obstacles of the development of remote sensing applications. To improve the accuracy of hyperspectral image analysis, the decomposition of the mixed pixels is required. This decomposition process is termed as (spectral) unmixing [9]–[11]. More precisely, spectral unmixing aims at extracting several pure endmember spectra from an observed mixed pixel and figuring out their corresponding abundance fractions [12].

*Corresponding author. Tel./fax: +86-021-54345187.

G. Zhang, Y. Xu and F. Fang are with the Shanghai Key Laboratory of Multidimensional Information Processing, and with the Department of Computer Science & Technology, East China Normal University, Shanghai, China. e-mails: {gxzhang, fmfang}@cs.ecnu.edu.cn, yyxu@ecnu.cn.

A. Related work

In the last few decades, a large number of unmixing techniques have been developed. Considering whether the secondary reflections and multiple scattering among different endmembers are negligible or not, the mixture models can be divided into two categories: linear mixture model and nonlinear mixture model. In the linear model, it is assumed that the hyperspectral data is a linear combination of some endmembers, while more complicated assumptions are adopted in nonlinear model. Since the linear mixture model is simple and effective in most real scenarios [13], we focus on the linear mixture model in this paper.

On the other hand, unmixing approaches can be roughly classified into supervised, unsupervised and semi-supervised methods according to our priori knowledge of the endmembers [14]: a) Supervised unmixing aims to estimate the abundances with known endmembers. The most classical and widely used abundance estimation algorithm is the fully constrained least squares (FCLS) method [15]. b) In unsupervised unmixing, both endmember signatures and their abundances are directly estimated from the observed data. We can first identify the endmember signatures use endmember extraction algorithms [16]–[20], then quantify the abundances of each estimated endmember using supervised unmixing methods. Moreover, simultaneously estimation can be realized using unsupervised FCLS [7], independent component analysis methods [21], [22], and non-negative matrix factorization based methods [23]–[27], etc. c) Semi-supervised unmixing takes the spectral library as a prior knowledge, then selects a proper subset of signatures from the library which can model each mixed pixel optimally [12]. Most of these methods are developed based on sparse regression [28]–[31], greedy algorithms [32], and Bayesian methods [33].

Generally, supervised unmixing methods could achieve a good estimation of abundances. However, the requirement for a priori knowledge of the endmember signatures have limited the application of these methods. As opposed to supervised unmixing, unsupervised unmixing methods directly unmix the given data without prior knowledge. Whereas, it also has some limitations: one is that endmember extraction algorithms always rely on some restrict assumptions, such as the pixel purity assumption, which are difficult to be guaranteed in practical applications [16]–[18]; the other is

This article has been accepted for publication in a future issue of this journal, but has not been fully edited. Content may change prior to final publication. Citation information: DOI 10.1109/TIP.2016.2523345, IEEE Transactions on Image Processing

that the abundances estimation may have a large cumulative error when the estimated endmembers are not precise [34]. On the contrary, semi-supervised unmixing methods avoid the above limitations by taking advantage of a spectral library. When spectral libraries are used, the abundances estimation procedure no longer depends on some strict assumptions nor on the capacity of the endmember extraction algorithms [12]. Due to those advantages, we focus on the semi-supervised unmixing in this paper.

A simple way to formulate the semi-supervised unmixing is to transform FCLS model into a semi-supervised fashion [12] by replacing the prior endmembers with a spectral library. However, since FCLS is formulated as a least squares problem constrained by the abundance sum-to-one and nonnegative constraints, it comes with the drawback of sensitive to noise. Actually, noise is somewhat inevitable in real conditions, which will interfere with the abundance estimation and bring adverse effects to unmixing results in terms of accuracy [12]. To address this issue, a possible solution is that we can adopt a denoising method, such as maximum noise fraction (MNF) transformation [35] or BM3D [36], in the preprocessing stage of an unmixing task. This idea can help FCLS unmixing to some extent. However, since MNF denoising has difficulty in achieving good balance between noise removal and detail preservation, it possibly results in a loss of useful information. While BM3D denoising relies on prior knowledge of accurate noise variance, whereas a perfect noise variance estimation is difficult in practice [37], and the inaccuracy of noise variance estimation could lead to an unsatisfactory denoise performance. Thus the improvement effect of the pre-denoised unmixing is limited. In practice, as stated in some literatures [38], unmixing is also helpful for denoising while preserving data's information. That is, unmixing and denoising can be promoted mutually. A good unmixing method should possess the property to resist noise. Thus, a reasonable choice may be a simultaneous procedure of unmixing and denosing.

In the past few years, many semi-supervised sparse unmixing methods have been developed in the framework of sparse representation. Taking advantage of sparse optimization, sparse unmixing models possess the capability of anti-noise. The main reason is three fold [39]. First, signal could be represented by few atoms while noise could not. Second, we can reject noise to some extent by selecting endmembers from the noiseless spectral library. Third, sparse regression optimization stops when the representation error reaches a pre-defined small value in order not to reconstruct noise [40]. Some prominent sparse unmixing methods are briefly introduced as follows. In 2010, Bioucas et al. proposed a sparse unmixing via variable splitting and augmented Lagrangian (SUnSAL) algorithm to solve an optimization problem regularized by ℓ_1-norm based sparsity term [28]. In 2012, SUnSAL-TV model includeing the total variation (TV) regularization to the classical sparse regression formulation [29] was proposed. It further improves the unmixing accuracy by assuming neighboring pixels have similar abundance for each endmember. In 2013, DSUnADM was developed to solve the sparse unmixing problem efficiently by applying a new alternating direction method (ADM) [41]. In 2014, collaborative SUnSAL (CLSUnSAL) was raised to solve the sparse unmixing problem using joint sparse regression [30]. Joint sparsity constraint assumes that the neighboring pixels share the similar endmembers which is less strict than TV regularization [8]. In summary, all the above sparse unmixing methods endeavor to exploit more efficient regularization terms to help unmixing.

B. Contribution

To further improve the unmixing performance on noisy hyperspectral data, we propose a new semi-supervised unmixing model termed framelet based sparse unmixing (FSU) in this paper. The construction of FSU model utilizes the sparse property of framelet representation. Different from the standard least-squares data fidelity term, a more effective one taking advantage of framelet transformation is exploited. Due to the fact that framelet representation enables us to discriminate the approximation and the detail components, the proposed method could better suppress noise during unmixing process by flexibly balancing the trade-off between these two parts. Besides, we develop an effective algorithm based on split Bregman algorithm to solve FSU model. Both the existence and uniqueness of the solution for our model and the convergence property of the proposed algorithm will be proved.

The rest of the paper is organized as follows. In Section II, we introduce the linear spectral unmixing model and semi-supervised unmixing formulation. A brief introduction of framelet and the proposed unmixing model are addressed in Section III. The numerical scheme with its convergence property are presented in Section IV. Various experiments on synthesized and real hyperspectral data are then reported in Section V to illustrate the superior performance of our approach. Finally, some concluding remarks are given in Section VI.

II. The Representation of Linear Mixture Model

Given an observed hyperspectral image $\bar{Y} \in \mathbb{R}^3$ with size of $b \times r \times c$, where b is the number of spectral bands, r and c are the rows and columns of the image in one band, we reshape $\bar{Y}$ to $Y \in \mathbb{R}^2$ with size of $b \times p$, where $p = r \times c$ is the number of pixels, and each column of Y represents the spectrum of a pixel.

Then the linear mixture model can be written as

$$Y = \tilde{A}H + \epsilon \tag{1}$$

where $\tilde{A} = [\tilde{\boldsymbol{a}}_1, \cdots, \tilde{\boldsymbol{a}}_j, \cdots, \tilde{\boldsymbol{a}}_e] \in \mathbb{R}^2$ (size: $b \times e$) is the endmember signatures matrix, each column $\tilde{\boldsymbol{a}}_j$ is b dimensional vector that denotes the spectral signature of the j-th endmember in the given image, e is the number of endmembers. $H = [\boldsymbol{h}_1, \cdots, \boldsymbol{h}_i, \cdots, \boldsymbol{h}_e]^T \in \mathbb{R}^2$ (size: $e \times p$) is the abundance fractions matrix, each row $\boldsymbol{h}_i$ is p dimensional vector that denotes the abundance of the i-th endmember in each pixel. ϵ denotes the additive noise.

In practice, it has been found that there are some properties in H, such as, 1) H is nonnegative, i.e., $H \geq 0$; 2) the sum of each column of H is one [7], [42], i.e., $\sum_{i=1}^{e} H_{i,j} = 1$

This article has been accepted for publication in a future issue of this journal, but has not been fully edited. Content may change prior to final publication. Citation information: DOI 10.1109/TIP.2016.2523345, IEEE Transactions on Image Processing

for each pixel $j = 1, \cdots, p$. Here $H_{i,j}$ denotes the (i,j)-th element of H.

Semi-supervised unmixing reformulate (1) by replacing $\tilde{A}$ with a spectral library $A \in \mathbb{R}^2$ (size: $b \times m$) as follows

$$Y = AH + \epsilon. \tag{2}$$

Here m is the number of spectral signatures in A, and $H = [\boldsymbol{h}_1, \cdots, \boldsymbol{h}_i, \cdots, \boldsymbol{h}_m]^T \in \mathbb{R}^2$ (size: $m \times p$) is an expansion of its previous version. Generally, m is much larger than e. In (2), all pixels of Y are supposed to share a small subset of endmembers, i.e., only a small number of columns in A contribute to combining the observed data, which means H has a small number of nonzero components. Therefore, semi-supervised unmixing aims at obtaining a sparse solution for H.

III. Proposed Unmixing Model

In this section, before presenting the proposed unmixing model, we first give a brief introduction to the framelet system. For simplicity, we only show the framelets in the univariate setting, and the framelets in the bivariate setting can be obtained by tensor product of the univariate one. Those who are interested in the framelets can refer to [43]–[45] for more details.

A. Framelets and image representation

Let $\chi \subset L^2(\mathbb{R})$ be a countable function subset, if

$$f = \sum_{g \in \chi} \langle f, g \rangle g, \quad \forall f \in L^2(\mathbb{R}),$$

or equivalently represented as

$$\|f\|^2_{L^2(\mathbb{R})} = \sum_{g \in \chi} |\langle f, g \rangle|^2, \quad \forall f \in L^2(\mathbb{R}),$$

where $\langle \cdot, \cdot \rangle$ is the inner product in $L^2(\mathbb{R})$, and $\| \cdot \|_{L^2(\mathbb{R})} = \langle \cdot, \cdot \rangle^{1/2}$ is the norm in $L^2(\mathbb{R})$. Then χ is called a tight frame of $L^2(\mathbb{R})$.

The tight frame is a generation of the orthogonal basis which relaxes the requirements of the orthogonality and linear independence [46]. It brings redundancy that leads to robust signal representations and helps unmixing of noisy data.

Given a finite set $\Phi = \{\phi^1, \cdots, \phi^r\} \subset L^2(\mathbb{R})$, the collection of dilations and shifts of Φ is called a wavelet system $\chi(\Phi)$, here

$$\chi(\Phi) = \{2^{k/2}\phi^j(2^k x - l) : 1 \le j \le r; k, l \in \mathbb{Z}\}.$$

When $\chi(\Phi)$ forms a tight frame, it is termed as a wavelet tight frame, and ϕ^j is a (tight) framelet.

To construct wavelet tight frames, one starts from a compactly supported refinable function (a scaling function) $\psi \in L^2(\mathbb{R})$ with a refinement mask (low-pass filter) $\xi_0 \in L^2(\mathbb{Z})$ satisfying a refinement equation

$$\psi(x) = \sum_{l \in \mathbb{Z}} \xi_0(l)\psi(2x - l).$$

Then, for the given compactly supported refinable function, a tight framelet system can be constructed by finding an appropriate set of framelets $\Phi = \{\phi^1, \cdots, \phi^r\} \subset L^2(\mathbb{R})$. Let $\{\xi_1, \cdots, \xi_r\} \subset L^2(\mathbb{Z})$ be a set of framelet masks (high-pass filters), then the framelets are defined as

$$\phi^j = \sum_{l \in \mathbb{Z}} \xi_j(l)\psi(2x - l), \quad j = 1, \cdots, r.$$

Thus, the construction of framelets Φ amounts to design the filters $\xi_0, \xi_1, \cdots, \xi_r$.

The unitary extension principle (UEP) in [47] gives the condition for $\chi(\Phi)$ to form as a tight frame system, i.e., the filters $\xi_0, \xi_1, \cdots, \xi_r$ satisfy

$$\zeta_{\xi_0}(\omega)\overline{\zeta_{\xi_0}(\omega + \gamma\pi)} + \sum_{j=1}^{r} \zeta_{\xi_j}(\omega)\overline{\zeta_{\xi_j}(\omega + \gamma\pi)} = \delta(\gamma), \quad \gamma = 0, 1,$$

for almost all $\omega \in \mathbb{R}$. Here $\zeta_\xi(\omega) = \sum_l \xi(l)e^{il\omega}$ and $\delta(\gamma)$ is a delta function.

Based on the UEP, a piecewise linear B-spline can be used as the refinable function ψ. The refinement mask is $\xi_0 = [\frac{1}{4}, \frac{1}{2}, \frac{1}{4}]$, and the two corresponding high-pass filters are

$$\xi_1 = [-\frac{1}{4}, \frac{1}{2}, -\frac{1}{4}], \quad \xi_2 = [\frac{\sqrt{2}}{4}, 0, -\frac{\sqrt{2}}{4}].$$

In the numerical scheme of image processing, the framelet transform (decomposition operator) can be represented by a matrix $\mathcal{W}$. The processes of generating such matrices have been detailed in many literatures such as [44]. We omit them here for readability.

One of the most important property of $\mathcal{W}$ is that it can be written as

$$\mathcal{W} = \begin{bmatrix} \mathcal{W}_0 \\ \mathcal{W}_1 \end{bmatrix}, \tag{3}$$

where $\mathcal{W}_0$ denotes the low-pass filter operator, and $\mathcal{W}_1$ consists of remaining band-pass and high-pass filter operators. Based on the UEP, the following equation holds

$$\mathcal{W}^T\mathcal{W} = \mathcal{W}_0^T\mathcal{W}_0 + \mathcal{W}_1^T\mathcal{W}_1 = \mathcal{I}, \tag{4}$$

where $\mathcal{W}^T$ and $\mathcal{I}$ are the inverse framelet transform and equivalent transform, respectively. Using $\mathcal{W}$, the framelet transformation (decomposition) process can be easily described. Given an hyperspatial image Y, the framelet coefficient vector X is given by

$$X = \mathcal{W}Y = \begin{bmatrix} \mathcal{W}_0 Y \\ \mathcal{W}_1 Y \end{bmatrix}, \tag{5}$$

where $\mathcal{W}_0 Y$ and $\mathcal{W}_1 Y$ are the approximation and detail coefficients, respectively. Besides, the framelet reconstruction process can be expressed as

$$Y = \mathcal{W}^T X = \left[\mathcal{W}_0^T X, \mathcal{W}_1^T X\right],$$

More importantly, the tight frame $\mathcal{W}$ satisfies $Y = \mathcal{W}^T\mathcal{W}Y$. That is, $\mathcal{W}^T\mathcal{W} = \mathcal{I}$. Generally, $\mathcal{W}\mathcal{W}^T \neq \mathcal{I}$, unless in the orthogonal case.

Finally, it should be noted that we work in the bivariate case for our unmixing work. The corresponding transform matrix can be readily obtained by the Kronecker product of the matrix corresponding to the univariate one (see [48] for details). In the following, we still use the notation $\mathcal{W}$ to denote the bivariate

This article has been accepted for publication in a future issue of this journal, but has not been fully edited. Content may change prior to final publication. Citation information: DOI 10.1109/TIP.2016.2523345, IEEE Transactions on Image Processing

framelet transform. We further note that $\mathcal{W}$ is used only for notational convenience. In the real numerical computation, we use fast algorithms for $\mathcal{W}Y$ and $\mathcal{W}^T X$, which only need to convolve with images using a couple of filters (see [48]).

Fig. 1 gives an intuitive example of framlelet decomposition. In detail, Fig. 1(a) is a subimage of the well-known AVIRIS Cuprite data set[1]; Fig. 1(b) shows the framelet coefficients after one level decomposition, in which the approximation coefficients are shown in the top left corner, and the detail coefficients are shown in the other parts; the histogram of Fig. 1(a) is shown in Fig. 1(c); and the histogram of the approximation coefficient value is shown in Fig. 1(d). Obviously, the histogram of approximation coefficient value is very similar to that of the original image. Fig. 1(e) and Fig. 1(f) are the histogram and the accumulative histogram of Fig. 1(b), respectively. We can observe from the two sub-figures that most of the framelet coefficient values are very small (almost 88% coefficient values are lower than 100). That is, most of the framelet coefficient values are equal to or very close to 0. Thus the hyperspectral images have sparse representations or approximations in the framelet domain.

B. Framelet based sparse unmixing model

We now propose a novel unmixing model by emphasizing both framelet-based sparsity (regularization term) and robust reconstruction (fidelity term). The principal effect of sparsity term is to preserve the sparse property of framelet coefficient value of abundance, and the reconstruction term, which will be split into two components in framelet domain, is used to reduce the interference of the additive noise.

In the following, we will detail the regularization and fidelity terms, then build the total unmixing model.

Firstly, we describe the two regularization terms based on two aforementioned properties, i.e., nonnegativity and sparsity, of the abundance matrix H.

- *Nonnegativity:* The nonnegative property of H can be represented by the following approach:

$$\min_H \|\iota(H)\|_{1,1} := \sum_{i,j} |\iota(H_{i,j})|,$$

where

$$\iota(H_{i,j}) = \begin{cases} 0, & H_{i,j} \geq 0 \\ +\infty, & \text{otherwise} \end{cases}.$$

- *Sparsity:* As explained in Section II, in semi-supervised unmixing, the fractional abundances denoted by H is a sparse matrix, which leads to the minimization of $\|H\|_{1,1}$. In addition, as illustrated in the previous subsection, an image usually have sparse approximations in the framelet domain [45]. The abundance maps can be viewed as the images that demonstrate the distributions and proportions of correspond endmembers. Thus they also have sparse property in framelet domian, suggesting that $\|\mathcal{W}H\|_{1,1}$ need to be minimized. Obviously, $\|\mathcal{W}H\|_{1,1} = \|\mathcal{W}_0 H\|_{1,1} + \|\mathcal{W}_1 H\|_{1,1}$ (see (5)). Since $\mathcal{W}_0$ is the low-pass filter operator (see (3)), $\mathcal{W}_0 H$ is roughly approximates to H (see Fig.1(c) and (d) for example). That is, $\|\mathcal{W}H\|_{1,1} \approx \|H\|_{1,1} + \|\mathcal{W}_1 H\|_{1,1}$, i.e., the first sparse property ($\min_H \|H\|_{1,1}$) is approximately included in the second one ($\min_H \|\mathcal{W}H\|_{1,1}$). Accordingly, the above two sparse properties can be simply illustrated by the second sparse term, i.e,

$$\min_H \|\mathcal{W}H\|_{1,1}. \tag{6}$$

On the other hand, due to the nature of the framelet transform, when we decompose the image Y into framelet domain (as shown in (5) and Fig. 1), the approximation coefficient value $\mathcal{W}_0 Y$ includes the majority of the image energy, while the detail coefficient value $\mathcal{W}_1 Y$ contains the detail information as well as most of the additive noise. In other words, the information and the noise of Y are mainly presented in $\mathcal{W}_0 Y$ and $\mathcal{W}_1 Y$, respectively. To verify those analysis, we

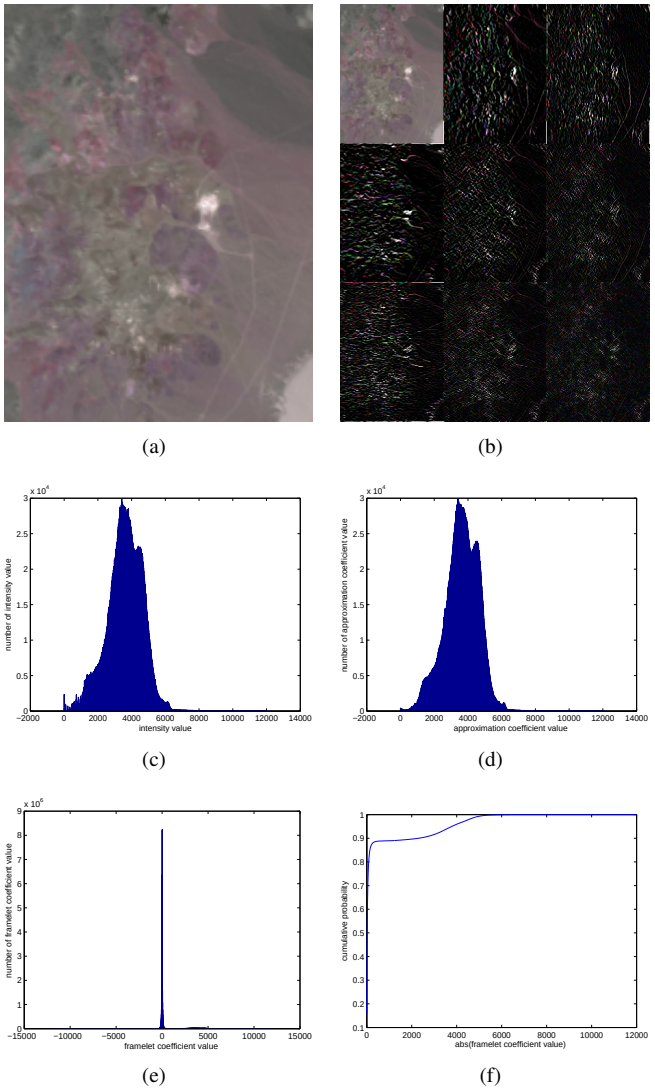

Fig. 1. An example of framelet decomposition. (a) the original image (RGB composite of the AVIRIS Cuprite subimage using bands 183, 193, and 203); (b) the result of one level framelet decomposition; (c) the histogram of the original image; (d) the histogram of the approximation coefficient value; (e) the histogram of the framelet coefficient value; (f) cumulative probability distribution corresponding to (e).

[1]Available online at http://aviris.jpl.nasa.gov/html/aviris.freedata.html

This article has been accepted for publication in a future issue of this journal, but has not been fully edited. Content may change prior to final publication. Citation information: DOI 10.1109/TIP.2016.2523345, IEEE Transactions on Image Processing

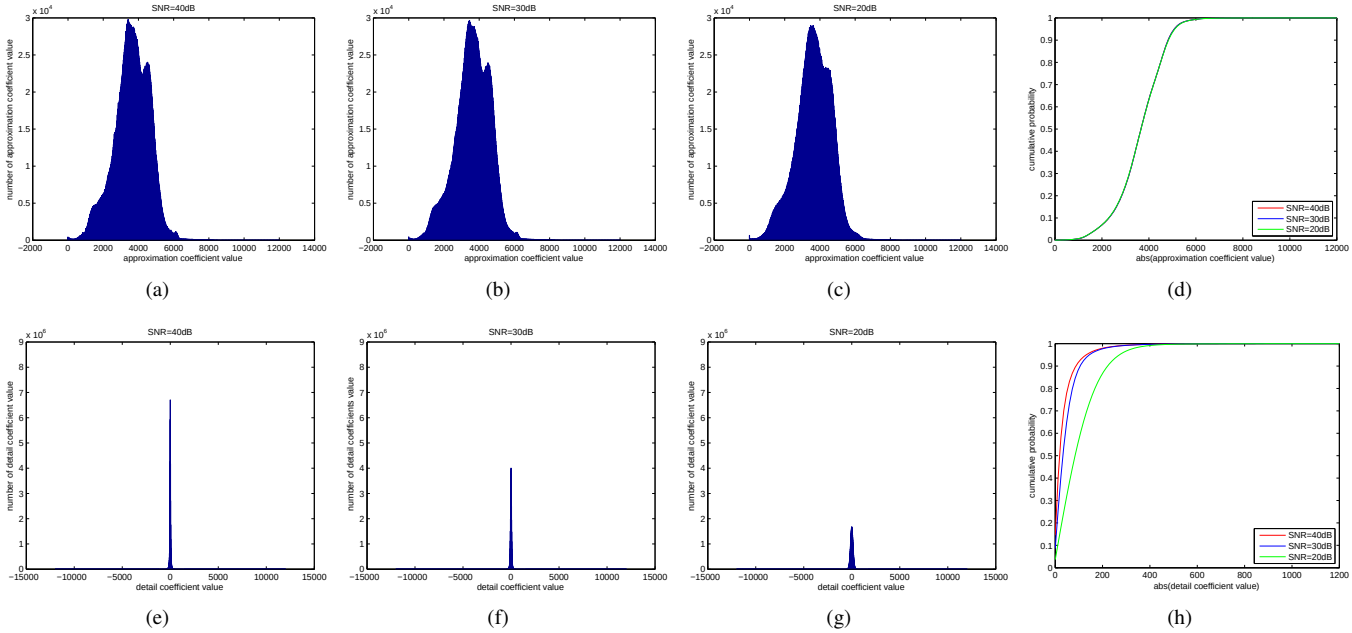

Fig. 2. The histograms of the framelet coefficient value of Cuprite data. (a)-(c) the histograms of approximate coefficient value when SNR=40, 30, and 20 dB, respectively; (d) the cumulative probability distributions corresponding to (a)-(c); (e)-(g) the histograms of detail coefficient value when SNR=40, 30, and 20 dB, respectively; (h) the cumulative probability distributions corresponding to (e)-(g).

respectively add the Gaussian noise to the Cuprite subimage (see Fig. 1(a)) with SNR=40 dB, 30 dB, and 20 dB[2], and decompose them into framelet coefficients. The histograms of the framelet coefficient value are shown in Fig. 2. It is clear, at different noise levels, that the histograms of approximation coefficient value are similar, while the histograms of detail coefficient value are significantly distinct with each other. That is, the noise has little influence on approximation parts. This observation motivates us to treat the approximation and detail parts separately, and formulate our fidelity term as:

$$\frac{1}{2}\left\|\begin{bmatrix}\mathcal{W}_0(AH-Y)\\ \sqrt{\alpha}\mathcal{W}_1(AH-Y)\end{bmatrix}\right\|_F^2.$$

It is equivalent to:

$$\frac{1}{2}\|\mathcal{W}_0AH-\mathcal{W}_0Y\|_F^2+\frac{\alpha}{2}\|\mathcal{W}_1AH-\mathcal{W}_1Y\|_F^2, \tag{7}$$

where $\|\cdot\|_F$ denotes the Frobenius norm, and $\alpha>0$ is a balance parameter. The first term of (7) requires that the approximation coefficient value of the observed Y should be close to that of the reconstructed AH. As for the second term, when the noise level of Y is low (i.e., SNR is high), the detail coefficient value of Y and AH can be sufficiently close. However, in the high noise situation, the requirement of minimizing this term is less strict as we tend to obtain a noiseless reconstructed image. Thus, α can be flexibly adjust to images with different noise levels, and a small α is preferred for the high noise situation.

Taking all the above terms into account, we can formulate our unmixing problem as the following optimization function:

$$\begin{aligned}\min_H E(H) =&\frac{1}{2}\|\mathcal{W}_0AH-\mathcal{W}_0Y\|_F^2+\frac{\alpha}{2}\|\mathcal{W}_1AH-\mathcal{W}_1Y\|_F^2\\ &+\beta\|\mathcal{W}H\|_{1,1}+\|\iota(H)\|_{1,1},\end{aligned} \tag{8}$$

where $\beta>0$ is a parameter.

Besides, we can readily prove the existence and uniqueness of the solution for (8).

Theorem 1. *Let $Y,A,H\in\mathbb{R}^2$, and $\alpha,\beta>0$, then the minimization problem* (8) *admits a unique solution in $\mathbb{R}^2$.*

Proof: Since $\mathcal{W},\mathcal{W}_0$ and $\mathcal{W}_1$ are linear operators, we can readily confirm the convexities of $\frac{1}{2}\|\mathcal{W}_0AH-\mathcal{W}_0Y\|_F^2$ and $\frac{\alpha}{2}\|\mathcal{W}_1AH-\mathcal{W}_1Y\|_F^2$. Besides, $\beta\|\mathcal{W}H\|_{1,1}$ is strictly convex. To prove this theorem, we now just need to verify the convexity of $\|\iota(H)\|_{1,1}$. This convexity is also rather obvious due to the fact that the ℓ_1 norm $\|\cdot\|_{1,1}$ and the function $\iota(\cdot)$ are convex. Thus, (8) is strictly convex in $\mathbb{R}^2$, then it admits a unique solution. ■

IV. Numerical Algorithm

In this section, the numerical procedure of the proposed model will be implemented. It is known that the minimization problem (8) can be solved by many efficient methods, such as augmented Lagrangian method [49], split Bregman algorithm [50], alternating direction method of multipliers (ADMM) [51], and Chambolle's algorithm [52]. In this paper, we adopt the multiple-splitting split Bregman algorithm.

As introduced in [50], the split Bregman algorithm, which has been proven to be equivalent to ADMM when dealing with the optimization problem with linear constraints [51], extends the utility of the Bregman and linear Bregman iterations. It is a promising method which can solve our non-differentiable

[2]Here SNR stands for "signal-to-noise ratio" which is inversely related to the noise level. It is defined as: $\mathrm{SNR(dB)}=10\log_{10}\frac{\|AH\|_2^2}{\|\epsilon\|_2^2}$.

This article has been accepted for publication in a future issue of this journal, but has not been fully edited. Content may change prior to final publication. Citation information: DOI 10.1109/TIP.2016.2523345, IEEE Transactions on Image Processing

convex optimization problem effectively, and can reduce the time and space overhead significantly. The wide applications in many image processing issues, such as image denoising and deblurring [45], have also demonstrated the superiority of the split Bregman algorithm.

The key idea of the split Bregman algorithm is that it will separate the ℓ_1 and ℓ_2 components. Thus, we first rewrite (8) as the following equivalent constrained problem:

$$\begin{aligned}\min_{H,V_1,V_2,V_3} &\frac{1}{2}\|\mathcal{W}_0V_1-\mathcal{W}_0Y\|_F^2+\frac{\alpha}{2}\|\mathcal{W}_1V_1-\mathcal{W}_1Y\|_F^2\\ &+\beta\|V_2\|_{1,1}+\|\iota(V_3)\|_{1,1},\\ \text{subject to}&\begin{cases}V_1=AH\\ V_2=\mathcal{W}H\\ V_3=H\end{cases}.\end{aligned} \tag{9}$$

Let

$$V\equiv(V_1,V_2,V_3),$$

$$E(V)\equiv\frac{1}{2}\|\mathcal{W}_0V_1-\mathcal{W}_0Y\|_F^2+\frac{\alpha}{2}\|\mathcal{W}_1V_1-\mathcal{W}_1Y\|_F^2+\beta\|V_2\|_{1,1}+\|\iota(V_3)\|_{1,1},$$

and

$$G=\begin{bmatrix}A\\ \mathcal{W}\\ I\end{bmatrix},\qquad B=\begin{bmatrix}I&0&0\\0&I&0\\0&0&I\end{bmatrix},$$

where I is the identity matrix with proper size. Then, (9) can be rewritten in a compact form:

$$\min_{H,V}E(V),\quad\text{subject to}\quad BV=GH. \tag{10}$$

The regular split Bregman algorithm of (10) is as follows:

$$\begin{cases}(H^{(t+1)},V^{(t+1)})=\arg\min_{H,V}E(V)+\frac{\mu}{2}\|GH-BV-D^{(t)}\|_F^2, & (11)\\ D^{(t+1)}=D^{(t)}+BV^{(t+1)}-GH^{(t+1)}, & (12)\end{cases}$$

where $\mu>0$ is a preset constant and $D\equiv(D_1,D_2,D_3)$ denotes the lagrangian multiplier associated with the constraint in (10).

To obtain $H^{(t+1)}$ and $V^{(t+1)}$, we need to solve the sub-problem (11) with respect to H and V alternately until the convergence condition reached. However, as shown in [50], the ultimate optimal efficiency can also be guaranteed when iterating H and V with only one iteration. That is, we can split (11) and solve H and V separately. Thus, $H^{(t+1)}$ can be directly obtained from the following minimization problem:

$$\begin{aligned}H^{(t+1)}&=\arg\min_H\frac{\mu}{2}\|GH-BV^{(t)}-D^{(t)}\|_F^2\\ &=\arg\min_H\frac{\mu}{2}\|AH-V_1^{(t)}-D_1^{(t)}\|_F^2\\ &\quad+\frac{\mu}{2}\|\mathcal{W}H-V_2^{(t)}-D_2^{(t)}\|_F^2\\ &\quad+\frac{\mu}{2}\|H-V_3^{(t)}-D_3^{(t)}\|_F^2.\end{aligned} \tag{13}$$

Since (13) is differentiable, the optimality condition of $H^{(t+1)}$ is readily obtained by calculating its first variation, which yields:

$$\begin{aligned}H^{(t+1)}=&(A^TA+2I)^{-1}[A^T(V_1^{(t)}+D_1^{(t)})\\ &+\mathcal{W}^T(V_2^{(t)}+D_2^{(t)})+(V_3^{(t)}+D_3^{(t)})].\end{aligned} \tag{14}$$

Meanwhile, to solve $V^{(t+1)}$ from (11), we need to compute $V_1,\ V_2$, and V_3, respectively. Firstly, the optimization problem for V_1 is as follows:

$$\begin{aligned}V_1^{(t+1)}=&\arg\min_{V_1}\frac{1}{2}\|\mathcal{W}_0V_1-\mathcal{W}_0Y\|_F^2\\ &+\frac{\alpha}{2}\|\mathcal{W}_1V_1-\mathcal{W}_1Y\|_F^2+\frac{\mu}{2}\|AH^{(t+1)}-V_1-D_1^{(t)}\|_F^2.\end{aligned}$$

Its first variation is

$$(K+\mu)V_1=KY+\mu\left(AH^{(t+1)}-D_1^{(t)}\right) \tag{15}$$

where K is an operator which is defined as

$$K=\mathcal{W}_0^T\mathcal{W}_0+\alpha\mathcal{W}_1^T\mathcal{W}_1.$$

We have the following property for K:

Proposition 1. *Assume ξ_0 is the corresponding low-pass filter of $\mathcal{W}_0$, $\mathcal{F}$ is the fast Fourier transform (FFT), and $\mathcal{F}(\cdot)^T$ is the complex conjugate of $\mathcal{F}(\cdot)$, then, $\mathcal{F}(K)=(1-\alpha)\mathcal{F}(\xi_0)^T\mathcal{F}(\xi_0)+\alpha$.*

Proof: Thanks to (4), we deduce that

$$K=\mathcal{W}_0^T\mathcal{W}_0+\alpha\mathcal{W}_1^T\mathcal{W}_1=(1-\alpha)\mathcal{W}_0^T\mathcal{W}_0+\alpha I.$$

Then we have

$$\mathcal{F}(K)=(1-\alpha)\mathcal{F}\left(\mathcal{W}_0^T\mathcal{W}_0\right)+\alpha=(1-\alpha)\mathcal{F}(\mathcal{W}_0)^T\mathcal{F}(\mathcal{W}_0)+\alpha.$$

In numerical scheme, $\mathcal{F}(\mathcal{W}_0)$ is essentially the $\mathcal{F}(\xi_0)$. Therefore,

$$\mathcal{F}(K)=(1-\alpha)\mathcal{F}(\xi_0)^T\mathcal{F}(\xi_0)+\alpha.$$

■

Using FFT, we can obtain the closed form solution of V_1 from (15) directly,

$$V_1^{(t+1)}=\mathcal{F}^{-1}\left(\frac{\mathcal{F}(K)\odot\mathcal{F}(Y)+\mu\mathcal{F}\left(AH^{(t+1)}-D_1^{(t)}\right)}{\mathcal{F}(K)+\mu}\right),$$

where $\odot$ is dot product operator, and $\mathcal{F}^{-1}$ denotes the inverse FFT.

Secondly, to compute V_2, we need to solve the following optimization problem:

$$V_2^{(t+1)}=\arg\min_{V_2}\beta\|V_2\|_{1,1}+\frac{\mu}{2}\|\mathcal{W}H^{(t+1)}-V_2-D_2^{(t)}\|_F^2. \tag{16}$$

That is, V_2 can be readily obtained by the well-known soft thresholding [53]:

$$V_2^{(t+1)}=\max\{|\mathcal{W}H^{(t+1)}-D_2^{(t)}|-\frac{\beta}{\mu},0\}\frac{\mathcal{W}H^{(t+1)}-D_2^{(t)}}{|\mathcal{W}H^{(t+1)}-D_2^{(t)}|}. \tag{17}$$

Finally, the optimization problem of V_3 is

$$V_3^{(t+1)}=\arg\min_{V_3}\|\iota(V_3)\|_{1,1}+\frac{\mu}{2}\|H^{(t+1)}-V_3-D_3^{(t)}\|_F^2. \tag{18}$$

Then V_3 is given by

$$V_3^{(t+1)}=\max(H^{(t+1)}-D_3^{(t)},0). \tag{19}$$

Overall, taking all above analyses into account, we can summarize the complete numerical procedure for the proposed method. The detailed descriptions are shown in Algorithm 1.

This article has been accepted for publication in a future issue of this journal, but has not been fully edited. Content may change prior to final publication. Citation information: DOI 10.1109/TIP.2016.2523345, IEEE Transactions on Image Processing

Algorithm 1: the overall procedure for the proposed model

Input: spectral library A, observed data Y.

Initialize:

set $t=0$, $H^{(0)}=(A^TA)^{-1}A^TY$, $V_1^{(0)}=AH^{(0)}$, $V_2^{(0)}=\mathcal{W}H^{(0)}$, $V_3^{(0)}=H^{(0)}$, $D_1^{(0)}=D_2^{(0)}=D_3^{(0)}=0$; fix $\mu>0$, $\alpha>0$ and $\beta>0$.

Repeat:

$$H^{(t+1)}=(A^TA+2I)^{-1}[A^T(V_1^{(t)}+D_1^{(t)}) +\mathcal{W}^T(V_2^{(t)}+D_2^{(t)})+(V_3^{(t)}+D_3^{(t)})],$$

$$V_1^{(t+1)}=\mathcal{F}^{-1}\left(\frac{\mathcal{F}(K)\odot\mathcal{F}(Y)+\mu\mathcal{F}\left(AH^{(t+1)}-D_1^{(t)}\right)}{\mathcal{F}(K)+\mu}\right),$$

$$V_2^{(t+1)}=\max\{|\mathcal{W}H^{(t+1)}-D_2^{(t)}|-\frac{\beta}{\mu},0\}\frac{\mathcal{W}H^{(t+1)}-D_2^{(t)}}{|\mathcal{W}H^{(t+1)}-D_2^{(t)}|},$$

$$V_3^{(t+1)}=\max(H^{(t+1)}-D_3^{(t)},0),$$

$$D_1^{(t+1)}=D_1^{(t)}+V_1^{(t+1)}-AH^{(t+1)},$$

$$D_2^{(t+1)}=D_2^{(t)}+V_2^{(t+1)}-\mathcal{W}H^{(t+1)},$$

$$D_3^{(t+1)}=D_3^{(t)}+V_3^{(t+1)}-H^{(t+1)},$$

update iteration: $t=t+1$,

Until the stopping criterion is satisfied.

Output: abundances H.

The convergence of Algorithm 1 can be guaranteed by the following theorem:

Theorem 2. *Suppose the unique solution of* (8) *is* H^*. *Assume that* $\alpha,\beta,\mu>0$. *Then, the following property for Algorithm 1 holds:*

$$\lim_{t\to\infty}E(H^{(t)})=E(H^*).$$

Furthermore,

$$\lim_{t\to\infty}H^{(t)}=H^*.$$

Proof: As stated in the Theorem 1, (8) has a unique solution. Then, applying Theorem 3.2 in [54], the Theorem 2 is proved. ∎

In addition, we use the relative error as our stopping criterion. Generally, the relative error $\varepsilon(H^{(t)})$ is defined as

$$\varepsilon(H^{(t)})=\frac{\|H^{(t)}-H^{(t+1)}\|_F}{\|H^{(t)}\|_F}.$$

Given a preset positive small parameter ϱ, Algorithm 1 can be considered as reaching a steady state when $\varepsilon(H^{(t)})\le\varrho$ (we set $\varrho=10^{-4}$ in the following experiments).

Finally, we give some discussions for the computational complexity of Algorithm 1. The computation of framelet transform $\mathcal{W}$ is essentially the convolution, thus the complexity of $\mathcal{W}Y$ is $O(bp\log p)$ when uses FFT. Besides, the $(A^TA+2I)^{-1}$ can be computed outside the loop since A is known. Then the complexities of computing all variables are shown in Table I.

From Table I, it is obvious that the most time-consuming steps are the calculations of H, V_1, and V_2. Thus, the overall complexity is $O(m^2p)+O(bp\log p)+O(bmp)$. In practice, $\log p$ is generally much smaller than m. Therefore, the computational complexity of Algorithm 1 is $O((m+b)mp)$.

V. Experimental Results

In this section, we will illustrate the performance of our proposed FSU method on both simulated and real data. The unmixing results are compared with five state-of-the-art approaches, i.e. BM3D+FCLS, MNF+FCLS, CLSUnSAL [30], DSUnADM [41], and SUnSAL-TV [29]. Here, BM3D+FCLS and MNF+FCLS denote two-stage methods combined denoising algorithm and unmixing method, i.e., the hyperspectral image will preproccess by BM3D or MNF to obtain a denoised data [35], [36], then the denoised data will be unmixed by the semi-supervised FCLS method [28]. Specifically, the noise variance estimated by function 'evar'[3] is used as one of the input parameters of BM3D MATLAB software[4], and MNF denoising is processed using ENVI software. All the algorithms are implemented using MATLAB R2013a on a laptop PC equipped with Intel Core i7 CPU (2.70GHz) and 12 GB RAM memory, and it takes averagely 0.15 seconds to process a pixel for FSU.

A. Experiments with simulated data

In this subsection, two simulated hyperspectral data are used to evaluate the performance of our algorithm.

- The first data cube contains 170×170 pixels and 224 bands per pixel. It is generated according to formula (2) and using 4 endmembers which are randomly selected from a spectral library $A_1\in\mathbb{R}^{224\times240}$. Here, A_1 is a randomly selected subset from the Chapter 1 of United Stated Geological Survey (USGS) digital spectral library (splib06a)[5] $A\in\mathbb{R}^{224\times498}$, and it contains 240 materials with 224 spectrum bands ranging from 0.4 to 2.5 μm. The true abundances of the 4 endmembers are presented in Fig. 3. As shown in this figure, the abundances are designed in the shape of pie, and each pie slice has different fractional value. Besides, the background pixels are the uniform mixture of 4 endmembers. After obtaining the data cube, the data is respectively affected by the Gaussian white noise for three different levels, i.e., SNR=20 dB, 30 dB, and 40 dB.

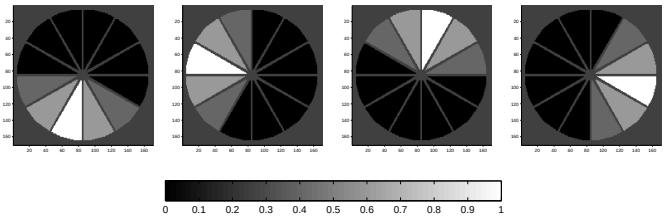

Fig. 3. True fractional abundance maps of selected four endmembers in the first simulated data cube.

- The second simulated data cube has 100×100 pixels and is composed of 9 randomly selected endmembers from a spectral library $A_2\in\mathbb{R}^{120\times100}$. A_2 is picked from a library which contains 262 spectral signatures from the NASA JSC Spacecraft Materials Spectral Database. The spectral signatures of this database can be generally found in real satellites, and has been used in many literatures [41]. The true fractional abundances of the 9

[3]Available online at http://www.biomecardio.com/matlab/evar.html

[4]Available online at http://www.cs.tut.fi/ foi/GCF-BM3D/

[5]Available online at http://speclab.cr.usgs.gov/spectral.lib06

This article has been accepted for publication in a future issue of this journal, but has not been fully edited. Content may change prior to final publication. Citation information: DOI 10.1109/TIP.2016.2523345, IEEE Transactions on Image Processing

TABLE I
THE COMPUTATIONAL COMPLEXITIES OF ALL VARIABLES IN ALGORITHM 1

H	V_1	V_2	V_3	D_1	D_2	D_3
$O(m^2p + mbp)$	$O(bp \log p + bmp)$	$O(bp \log p)$	$O(mp)$	$O(bp)$	$O(mp)$	$O(mp)$

endmembers (which has been used in [29], [41], [55]) are shown in Fig. 4. After generating the data cube, it is contaminated by Gaussian white noise using the same SNR values as the first data.

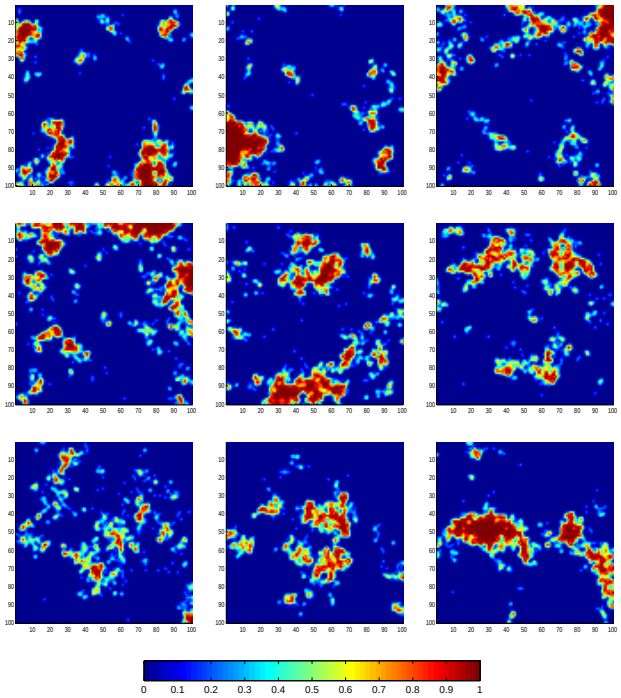

Fig. 4. True fractional abundance maps of selected nine endmembers in the second simulated data cube.

The unmixing performance of simulated data can be quantitatively evaluated by two metrics: signal to reconstruction error (SRE) and root mean square error (RMSE) [29], [30]. The two metrics are defined as:

$$\text{SRE} \equiv \frac{\mathbb{E}[\|H_{true}\|_F^2]}{\mathbb{E}[\|H_{true} - H\|_F^2]},$$

and

$$\text{RMSE} = \frac{1}{\sqrt{e \times p}} \mathbb{E}[\|H_{true} - H\|_F^2],$$

where H_{true} denotes the true fractional abundances of endmembers and H is the estimated fractional abundances of endmembers obtained by Algorithm 1. Generally, SRE is measured in dB: $\text{SRE(dB)} \equiv 10 \log_{10}(\text{SRE})$. Obviously, the higher SRE and lower RMSE value represent the better unmixing performance.

We now test our FSU model and the other five state-of-the-art approaches using the aforementioned two simulated data. All the parameters used in our experiments are selected from a candidate set: 0, 0.0005, 0.001, 0.005, 0.01, 0.05, 0.1, 0.3, 0.5, and 1. This parameters set has been used in [29], and has included the optimal parameters of all our compared algorithms as reported in their respective paper. Detailedly, the parameters of the compared algorithms are tuned to their optimal performances. As for FSU, we set the parameter pair (α, β) to (0.01, 0.05), (0.1, 0.01), and (1, 0.005) for 20 dB, 30 dB, and 40 dB noise levels, respectively. Notice that we increase α and decrease β when the data's SNR increases. This is reasonable since the noise is mainly contained in the high frequency term, and the duty of the regularization term is essentially to keep the sparse property (which can also suppress noise).

Figs. 5 and 7 show the estimated abundance maps of the six methods on the first and second simulated data sets, respectively. Since the abundance maps of different endmembers present similar estimated results, we only illustrate the 4-th endmember of the first data cube and the 1-st endmember of the second data cube as the representatives. In these two figures, the columns from left to right list the abundance maps estimated by BM3D+FCLS, MNF+FCLS, CLSUnSAL, DSUnADM, SUnSAL-TV, and FSU sequentially, and the rows from top to bottom present the results with SNR=40 dB, 30 dB, and 20 dB, respectively. It can be observed from the two figures that, for high SNR values (i.e., low noise levels), there are few differences among these six methods visually. However, the outperformance of FSU becomes more obvious when the SNR value decreases.

To see the differences of all the estimated abundances more clearly, taking the results of SNR=20 dB as examples, we present a visualization of the differences between ground truth and estimated abundances in two certain areas from Fig. 5 and Fig. 7, respectively. The close-ups of their difference images are shown in Fig. 6 and Fig. 8, darker pixel means smaller difference. It can be observed from Fig. 6 that most pixels in the difference images of FSU (Fig. 6(f)) are similar to BM3D+FCLS (Fig. 6(a)) and darker than others (Fig. 6(b)-(e)). Moreover, significant superiority of FSU can be seen from Fig. 8, where the difference images of FSU (Fig. 8(f)) are obviously darker than all others (Fig. 8(a)-(e)). That is, the abundance maps estimated by FSU are much closer to the ground truth than others in general.

The above observations can be quantitatively confirmed by the Tables II and III which record the SRE(dB) and RMSE values of the unmixing results of the two data sets. It can be seen that sparse unmixing methods are generally better than pre-denoised unmixing methods, and our FSU model obtains the highest SRE(dB) values and lowest RMSE values in most cases compared with the other five methods. It is worth noting that the performances of BM3D+FCLS and MNF+FCLS are significantly different with the two simulated data in the case of SNR=20 dB. Taking a closer look at Tables II and III, for the first simulated data, the SRE value of BM3D+FCLS is about 0.5 dB higher than FSU, and MNF+FCLS is more than

This article has been accepted for publication in a future issue of this journal, but has not been fully edited. Content may change prior to final publication. Citation information: DOI 10.1109/TIP.2016.2523345, IEEE Transactions on Image Processing

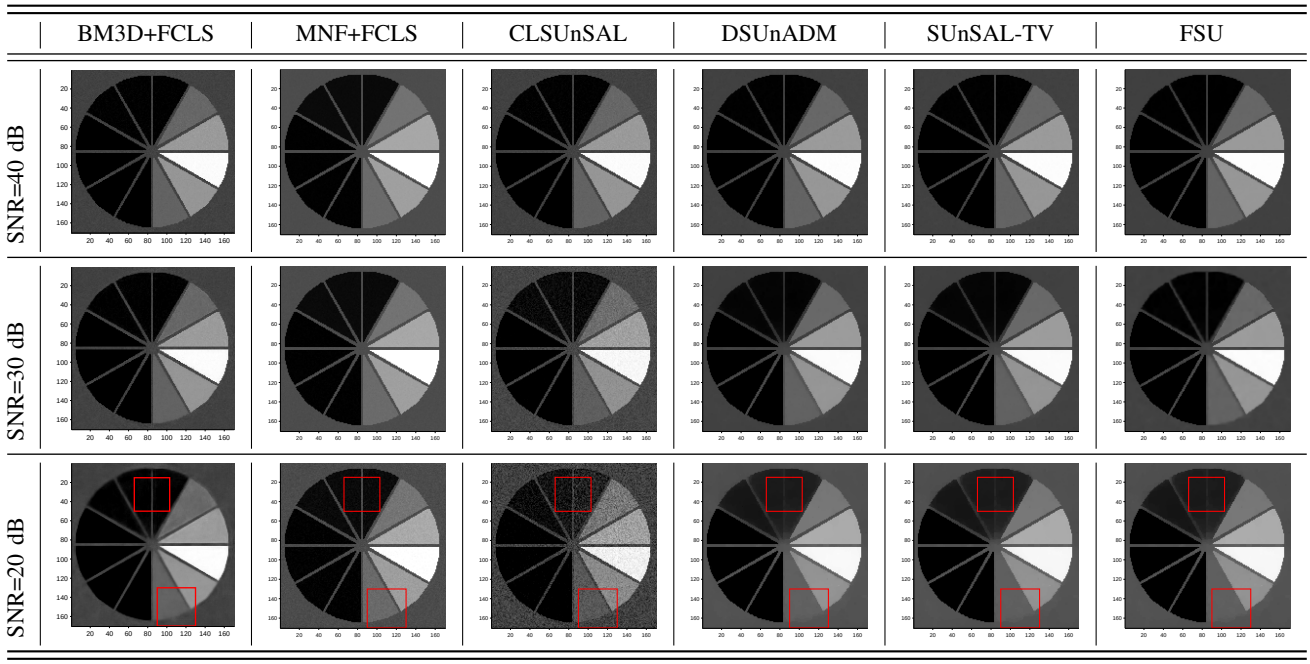

Fig. 5. The abundance maps estimated by BM3D+FCLS, MNF+FCLS, CLSUnSAL, DSUnADM, SUnSAL-TV, and FSU for the first simulated data cube (4-th endmember).

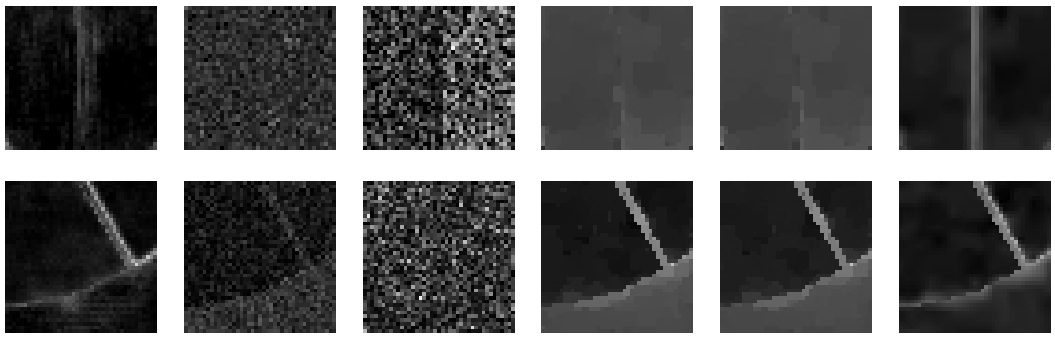

Fig. 6. The difference images of the regions in red boxes from Fig. 5. (a)-(f) are the difference images of BM3D+FCLS, MNF+FCLS, CLSUnSAL, DSUnADM, SUnSAL-TV, and FSU, respectively. We show quadrupled absolute values for better visual effect.

TABLE II
SRE(dB) AND RMSE VALUES OF DIFFERENT UNMIXING METHODS TO THE FIRST SIMULATED DATA CUBE ON DIFFERENT NOISE LEVELS

SNR		BM3D+FCLS	MNF+FCLS	CLSUnSAL	DSUnADM	SUnSAL-TV	FSU
40 dB	SRE	16.8935	15.5332	17.0848	21.3077	20.1629	**22.1251**
	RMSE	0.0066	0.0077	0.0064	0.0039	0.0045	**0.0036**
30 dB	SRE	15.3105	15.1620	9.1537	16.2862	16.0588	**18.0010**
	RMSE	0.0079	0.0080	0.0160	0.0070	0.0072	**0.0058**
20 dB	SRE	**13.3792**	11.8006	4.2865	9.2161	9.1457	12.8818
	RMSE	**0.0098**	0.0118	0.0280	0.0159	0.0160	0.0104

TABLE III
SRE(dB) AND RMSE VALUES OF DIFFERENT UNMIXING METHODS TO THE SECOND SIMULATED DATA CUBE ON DIFFERENT NOISE LEVELS

SNR		BM3D+FCLS	MNF+FCLS	CLSUnSAL	DSUnADM	SUnSAL-TV	FSU
40 dB	SRE	14.2389	15.5288	14.6597	18.1897	18.2274	**19.4870**
	RMSE	0.0141	0.0121	0.0134	0.0089	0.0089	**0.0077**
30 dB	SRE	8.6307	8.9188	8.1536	12.9399	12.9881	**14.6790**
	RMSE	0.0268	0.0260	0.0283	0.0163	0.0162	**0.0134**
20 dB	SRE	5.5624	1.9547	4.1745	7.2897	7.3858	**9.9667**
	RMSE	0.0382	0.0579	0.0448	0.0313	0.0310	**0.0230**

This article has been accepted for publication in a future issue of this journal, but has not been fully edited. Content may change prior to final publication. Citation information: DOI 10.1109/TIP.2016.2523345, IEEE Transactions on Image Processing

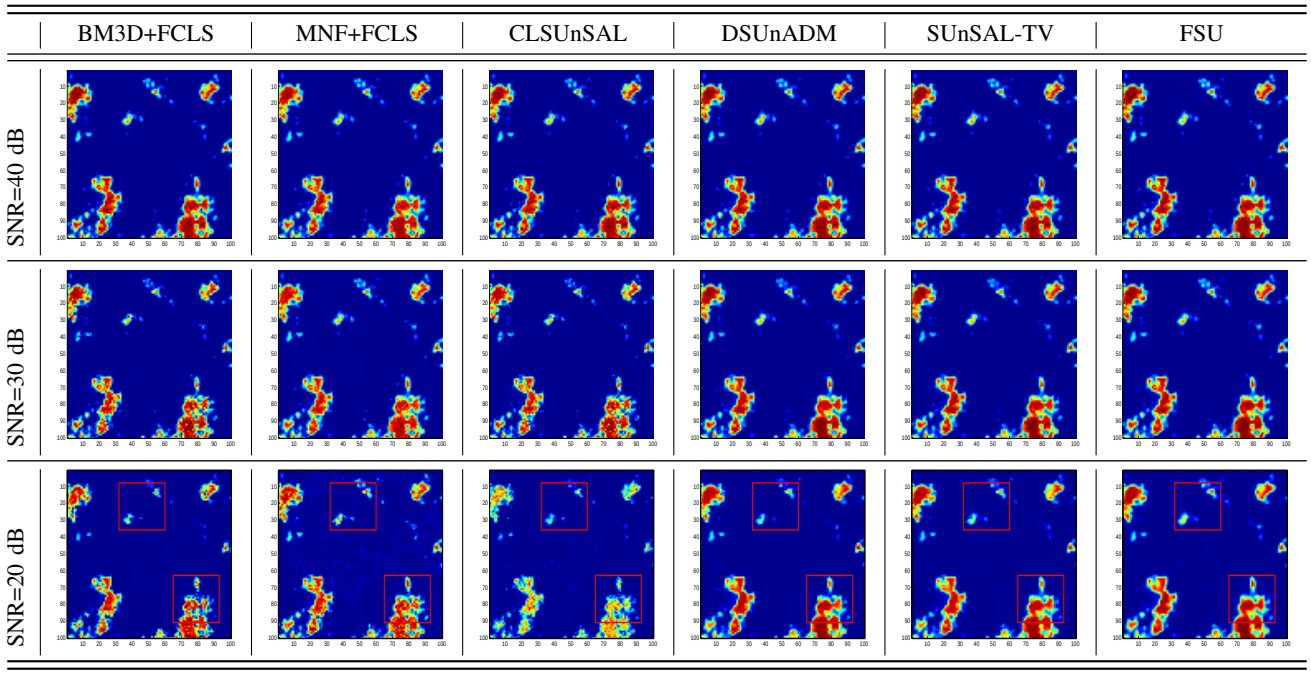

Fig. 7. The abundance maps estimated by BM3D+FCLS, MNF+FCLS, CLSUnSAL, DSUnADM, SUnSAL-TV, and FSU for the second simulated data cube (1-st endmember).

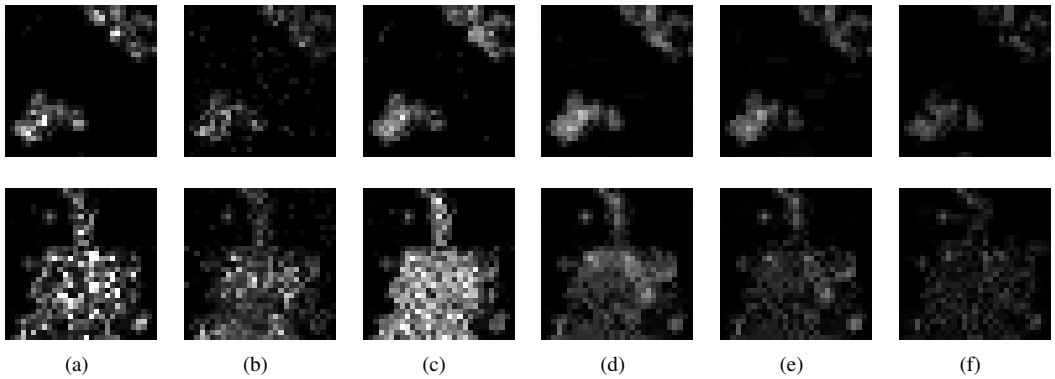

Fig. 8. The difference images of the regions in red boxes from Fig. 7. (a)-(f) are the difference images of BM3D+FCLS, MNF+FCLS, CLSUnSAL, DSUnADM, SUnSAL-TV, and FSU, respectively. We show doubled absolute values for better visual effect.

1 dB lower than FSU. However, for the second simulated data, the SRE value of BM3D+FCLS is about 4.4 dB lower than FSU, and MNF+FCLS is more than 8 dB lower than FSU. That is, the performances of BM3D+FCLS and MNF+FCLS are comparable with FSU on the first simulated data, whereas severely worse than FSU on the second simulated data. This phenomenon indicates that pre-denoised methods may be sensitive to the structural information presented in data, while FSU is more robust to different data.

Overall, it can be concluded that the improvements of our FSU model are significant both visually and quantitatively. For the two simulated data sets, our estimated abundance maps come closest to the ground truth in most cases, and the average increase of SRE values is 1.3 dB compared with the second best results. The encouraging results indicate that framelet transformation is beneficial to sparse unmixing.

B. Experiments with real data

In this part, the validity of our FSU model will be tested on the real hyperspectral data. Since the true abundance of each endmember in real data is unknown, we use the reconstruction error (RE) of the hyperspectral image and the sparsity of the abundances as two quantitative indexes [32]. Specifically, the RE reflects the difference between the original hyperspectral image and the one reconstructed by the actual endmembers and their estimated abundances, i.e., $\text{RE} = \sqrt{\frac{1}{b\times p}\times ||Y-AH||_F^2}$. It is may not a good measure for evaluating the unmixing performance, because it depends on the sparsity level, and favors the flexible and complex methods with very high representational capability. However, it still can roughly evaluates the abundances estimation for the actual endmembers when no ground truth is available [56]. On the other hand, the sparsity is evaluted by calculating the average proportion of zero entries in the abundance maps. The same as in [30] and [32], we regard the abundances smaller than 0.001 as negligible values

This article has been accepted for publication in a future issue of this journal, but has not been fully edited. Content may change prior to final publication. Citation information: DOI 10.1109/TIP.2016.2523345, IEEE Transactions on Image Processing

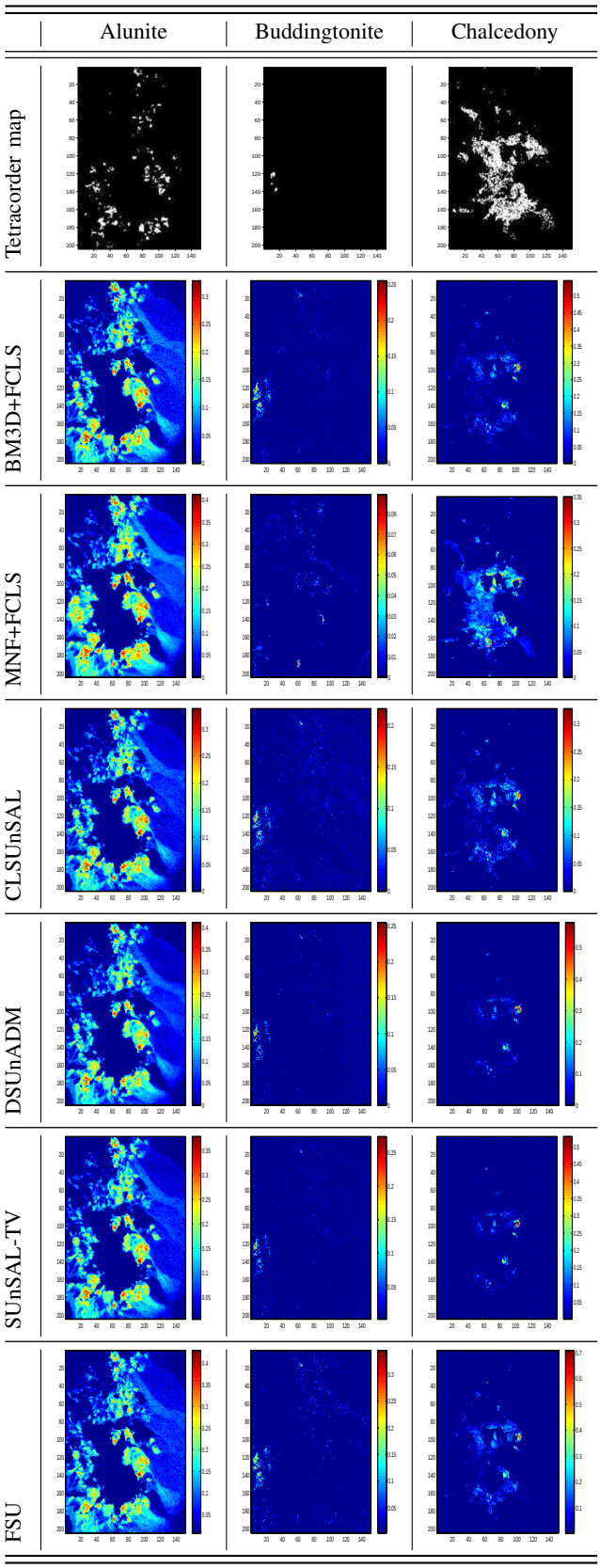

Fig. 9. The distribution maps produced by Tricorder software and the abundance maps estimated by BM3D+FCLS, MNF+FCLS, CLSUnSAL, DSUnADM, SUnSAL-TV, and FSU for the subset of the AVIRIS Cuprite scene at SNR=40 dB noise level.

and count them as zeros. Generally speaking, an unmixing algorithm that can obtain low reconstruction error as well as high sparsity of abundances is preferred.

The well-known AVIRIS Cuprite data set is used in our real data experiment. The portion used here is a subset of the Cuprite with the size of 204×151 pixels. Each pixel of the scene has 224 wavelength bands ranging from 0.4 to 2.5 μm. Fig. 1(a) shows a pseudo-colored composite of this data. We remove some low-SNR bands and water-vapor absorption bands (i.e., bands 1-2, 105-115, 150-170, and 223-224), leaving 188 bands for processing [12], [29]. Since the Cuprite data has very high signal to noise ratio after this preprocess, we test the proposed algorithm and all the competitors in the situation of SNR=40 dB noise level. Many previous works on this hyperspectral data have stated that there are about 14 kinds of mineral in this scene [18], [42]. Since the USGS digital spectral library (splib06a) A (have been mentioned in Section V-A) contains those 14 material signatures, we use the A with the corresponding low-SNR bands and water-vapor absorption bands removed as our spectral library.

Fig. 9 illustrates a qualitative comparison on the abundance maps for the three prominent minerals: *Alunite*, *Buddingtonite*, and *Chalcedony* produced by BM3D+FCLS, MNF+FCLS, CLSUnSAL, DSUnADM, SUnSAL-TV, and FSU. The parameters of the compared algorithms are tuned to their best performance, and the parameters α and β in our model are set to 0.01 and 0.001, respectively. The first row of Fig. 9 is the classification maps generated by USGS Tetracorder software. This map is a good indicator for qualitative assessment of the abundance maps produced by different unmixing methods [12]. It can be observed that all the estimated minerals roughly agree with the information provided by the USGS Tetracorder classification maps. Moreover, our proposed results visually have less noise than other considered methods. Specifically, compared with the others, the abundances estimated by FSU are generally comparable or higher for the respective minerals. This observation is particularly obvious for the abundances corresponding to the *Chalcedony*.

The quantitative evaluation results that shown in Table IV also confirm the better performance of the proposed method. It can be seen that FSU obtains both the lowest reconstruction error and the most sparse solution, which indicate that our method can use the actual endmembers to explain the data effectively. Therefore, we can concluded that FSU is effective for unmixing real hyperspectral data.

VI. Conclusion

We have developed a new model called framelet based sparse unmixing (FSU) for hyperspectral unmixing by taking advantages of the framelet representations on the hyperspectral data and its abundances. The proposed model takes the nonnegative and sparse properties of the abundances as the regularization terms, and formulates the data fidelity term by considering the approximation and detail coefficient values of the original hyperspectral data in framelet domain separately. The existence and uniqueness of the solution for FSU model is then discussed. The split Bregman algorithm as well as

TABLE IV
THE RECONSTRUCTION ERRORS (RE) AND THE SPARSITY OF ABUNDANCES ON REAL DATA EXPERIMENT

Algorithms	BM3D+FCLS	MNF+FCLS	CLSUnSAL	DSUnADM	SUnSAL-TV	FSU
RE	0.0802	0.0243	0.0338	0.0088	0.0080	**0.0078**
Sparsity	0.6745	0.6641	0.6499	0.4293	0.6356	**0.6988**

its convergence property are presented to obtain the optimal solution efficiently. Extensive experiments are conducted on both simulated and real data, and the unmixing results of FSU model are compared with pre-denoised unmixing methods as well as state-of-the-art sparse unmixing methods. Both qualitative comparison and quantitative analysis prove that our model generally achieves more accurate unmixing results than others.

For simplicity, in the current model, we leave out the structural information of data itself. Since the data-guided structural information will certainly help the unmixing task, our further work will focus on the detailed analysis of the data-guided sparse unmixing. Besides, in most cases, there are only few materials exist in a certain scene. Therefore, the use of the complete spectral library is uneconomical. Another relevant topic deserving further study will be the effective spectral library pruning based on given hyperspectral data. Finally, as our method is a general framework, it can be extended in many possible ways, such as the application of curvelet and others. We also leave those as further works.

ACKNOWLEDGMENT

We would like to thank M.-D. Iordache, J. Bioucas-Dias, A. Plaza and X. Zhao for sharing their codes for algorithms of SUnSAL-TV, CLSUnSAL, and DSUnADM, and thank W. Tang for his helpful suggestions on our experiments. Besides, the authors would like to sincerely thank the reviewers for their valuable and constructive comments. This work is supported by the National Basic Research Program (973 Program, No. 2011CB707104), the National Science Foundation of China (61372147 and 61501188), the Science and Technology Commission of Shanghai Municipality under research grant no. 14DZ2260800, and the Science Foundation of Shanghai (15ZR1410200).

REFERENCES

[1] D. Manolakis, C. Siracusa, and G. Shaw, "Hyperspectral subpixel target detection using linear mixing model," *IEEE Transactions on Geoscience and Remote Sensing*, vol. 39, no. 7, pp. 1392–1409, 2001.

[2] C. Chang and D. Heinz, "Constrained subpixel target detection for remotely sensed imagery," *IEEE Transactions on Geoscience and Remote Sensing*, vol. 38, no. 3, pp. 1144–1159, 2000.

[3] L. Miao and H. Qi, "Endmember extraction from highly mixed data using minimum volume constrained nonnegative matrix factorization," *IEEE Transactions on Geoscience and Remote Sensing*, vol. 45, no. 3, pp. 765–777, 2007.

[4] D. Landgrebe, "Multispectral land sensing: Where from, where to?" *IEEE Transactions on Geoscience and Remote Sensing*, vol. 43, no. 3, pp. 414–421, 2005.

[5] N. Keshava, "A survey of spectral unmixing algorithms," *Lincoln Laboratory Journal*, vol. 14, pp. 55–78, 2003.

[6] T. Lillesand, R. W. Kiefer, and J. Chipman, *Remote sensing and image interpretation*. John Wiley & Sons, 2014.

[7] D. Heinz and C. Chang, "Fully constrained least squares linear spectral mixture analysis method for material quantification in hyperspectral imagery," *IEEE Transactions on Geoscience and Remote Sensing*, vol. 39, no. 3, pp. 529–545, 2001.

[8] Q. Qu, N. Nasrabadi, and T. Tran, "Abundance estimation for bilinear mixture models via joint sparse and low-rank representation," *IEEE Transactions on Geoscience and Remote Sensing*, vol. 52, pp. 4404–4423, 2014.

[9] J. Adams, M. Smith, and P. Johnson, "Spectral mixture modeling: A new analysis of rock and soil types at the viking lander 1 site," *Journal of Geophysical Research: Solid Earth*, vol. 91, no. B8, pp. 8098–8112, 1986.

[10] J. Broadwater and R. Chellappa, "Hybrid detectors for subpixel targets," *IEEE Transactions on Pattern Analysis and Machine Intelligence*, vol. 29, no. 11, pp. 1891–1903, 2007.

[11] W. Ma, J. Bioucas-Dias, T. Chan, N. Gillis, P. Gader, A. Plaza, A. Ambikapathi, and C. Chi, "A signal processing perspective on hyperspectral unmixing: Insights from remote sensing," *IEEE Signal Processing Magazine*, vol. 31, no. 1, pp. 67–81, 2014.

[12] M. Iordache, J. Bioucas-Dias, and A. Plaza, "Sparse unmixing of hyperspectral data," *IEEE Transactions on Geoscience and Remote Sensing*, vol. 49, no. 6, pp. 2014–2039, 2011.

[13] J. Bioucas-Dias and A. Plaza, "An overview on hyperspectral unmixing: Geometrical, statistical, and sparse regression based approaches," in *IEEE International Geoscience and Remote Sensing Symposium (IGARSS)*, 2011, pp. 1135–1138.

[14] K. Themelis, A. Rontogiannis, and K. Koutroumbas, "Semi-supervised hyperspectral unmixing via the weighted lasso," in *ICASSP*, 2010, pp. 1194–1197.

[15] D. Heinz, C. Chang, and M. Althouse, "Fully constrained least-squares based linear unmixing," in *IEEE 1999 International Geoscience and Remote Sensing Symposium*, vol. 2, 1999, pp. 1401–1403.

[16] J. Boardman, "Automating spectral unmixing of AVIRIS data using convex geometry concepts," in *Summaries of the 4th Annual JPL Airborne Geoscience Workshop*, vol. 1. JPL Publication, 1993, pp. 11–14.

[17] M. Winter, "N-findr: An algorithm for fast autonomous spectral endmember determination in hyperspectral data," in *Imaging Spectrometry V*, M. Descour and S. Shen, Eds., vol. 3753. SPIE Proceedings, 1999, pp. 266–275.

[18] J. Nascimento and J. Bioucas-Dias, "Vertex component analysis: A fast algorithm to unmix hyperspectral data," *IEEE Transactions on Geoscience and Remote Sensing*, vol. 43, no. 4, pp. 898–910, 2005.

[19] J. Li and J. Bioucas-Dias, "Minimum volume simplex analysis: A fast algorithm to unmix hyperspectral data," in *IEEE International Geoscience & Remote Sensing Symposium*, Boston, 2008, pp. 250–253.

[20] C. Chi, T. Chan, and W. Ma, "A convex analysis based minimum volume enclosing simplex algorithm for hyperspectral unmixing," in *International Conference on Acoustics, Speech, and Signal Processing*, Taiwan, 2009, pp. 1089–1092.

[21] J. Nascimento and J. Bioucas-Dias, "Does independent component analysis play a role in unmixing hyperspectral data?" *IEEE Transactions on Geoscience and Remote Sensing*, vol. 43, no. 1, pp. 175–187, 2005.

[22] J. Wang and C. Chang, "Applications of independent component analysis in endmember extraction and abundance quantification for hyperspectral imagery," *IEEE Transactions on Geoscience and Remote Sensing*, vol. 44, no. 9, pp. 2601–2616, 2006.

[23] V. Pauca, J. Piper, and R. Plemmons, "Nonnegative matrix factorization for spectral data analysis," *Linear Algebra and its Applications*, vol. 416, no. 1, pp. 29–47, 2006.

[24] S. Jia and Y. Qian, "Constrained nonnegative matrix factorization for hyperspectral unmixing," *IEEE Transactions on Geoscience and Remote Sensing*, vol. 47, no. 1, pp. 161–173, 2009.

[25] Z. Yang, G. Zhou, S. Xie, S. Ding, J. Yang, and J. Zhang, "Blind spectral unmixing based on sparse nonnegative matrix factorization,"

IEEE Transactions on Image Processing, vol. 20, no. 4, pp. 1112–1125, 2011.
[26] X. Lu, H. Wu, Y. Yuan, P. Yan, and X. Li, "Manifold regularized sparse NMF for hyperspectral unmixing," *IEEE Transactions on Geoscience and Remote Sensing*, vol. 51, no. 5, pp. 2815–2826, 2013.
[27] F. Zhu, Y. Wang, B. Fan, S. Xiang, G. Meng, and C. Pan, "Spectral unmixing via data-guided sparsity," *IEEE Transactions on Image Processing*, vol. 23, no. 12, pp. 5412–5427, 2014.
[28] J. Bioucas-Dias and M. Figueiredo, "Alternating direction algorithms for constrained sparse regression: Application to hyperspectral unmixing," in *2nd Workshop on Hyperspectral Image and Signal Processing: Evolution in Remote Sensing (WHISPERS)*, 2010, pp. 1–4.
[29] M. Iordache, J. Bioucas-Dias, and A. Plaza, "Total variation spatial regularization for sparse hyperspectral unmixing," *IEEE Transactions on Geoscience and Remote Sensing*, vol. 50, no. 11, pp. 4484–4502, 2012.
[30] ——, "Collaborative sparse regression for hyperspectral unmixing," *IEEE Transactions on Geoscience and Remote Sensing*, vol. 51, no. 2, pp. 341–354, 2014.
[31] W. Tang, Z. Shi, Y. Wu, and C. Zhang, "Sparse unmixing of hyperspectral data using spectral a priori information," *IEEE Transactions on Geoscience and Remote Sensing*, vol. 53, no. 2, pp. 770–783, 2015.
[32] W. Tang, Z. Shi, and Y. Wu, "Regularized simultaneous forward–backward greedy algorithm for sparse unmixing of hyperspectral data," *IEEE Transactions on Geoscience and Remote Sensing*, vol. 52, no. 9, pp. 5271–5288, 2014.
[33] K. Themelis, A. Rontogiannis, and K. Koutroumbas, "A novel hierarchical bayesian approach for sparse semisupervised hyperspectral unmixing," *IEEE Transactions on Signal Processing*, vol. 60, no. 2, pp. 585–599, 2012.
[34] X. Chen, J. Chen, X. Jia, B. Somers, J. Wu, and P. Coppin, "A quantitative analysis of virtual endmembers' increased impact on the collinearity effect in spectral unmixing," *IEEE Transactions on Geoscience and Remote Sensing*, vol. 49, no. 8, pp. 2945–2956, 2011.
[35] A. A. Green, M. Berman, P. Switzer, and M. D. Craig, "A transformation for ordering multispectral data in terms of image quality with implications for noise removal," *IEEE Transactions on Geoscience and Remote Sensing*, vol. 26, no. 1, pp. 65–74, 1988.
[36] K. Dabov, A. Foi, V. Katkovnik, and K. Egiazarian, "Image denoising by sparse 3-D transform-domain collaborative filtering," *IEEE Transactions on Image Processing*, vol. 16, no. 8, pp. 2080–2095, 2007.
[37] A. Huntbatch, S.-L. Lee, D. Firmin, and G.-Z. Yang, "Bayesian motion recovery framework for myocardial phase-contrast velocity mri," in *Medical Image Computing and Computer-Assisted Intervention–MICCAI 2008*. Springer, 2008, pp. 79–86.
[38] D. Cerra, R. Muller, and P. Reinartz, "Noise reduction in hyperspectral images through spectral unmixing," *IEEE Geoscience and Remote Sensing Letters*, vol. 11, no. 1, pp. 109–113, 2014.
[39] Y. Zhao and J. Yang, "Hyperspectral image denoising via sparse representation and low-rank constraint," *IEEE Transactions on Geoscience and Remote Sensing*, vol. 53, no. 1, pp. 296–308, 2015.
[40] J. Mairal, M. Elad, and G. Sapiro, "Sparse representation for color image restoration," *IEEE Transactions on Image Processing*, vol. 17, no. 1, pp. 53–69, 2008.
[41] X. Zhao, F. Wang, T. Huang, M. Ng, and R. Plemmons, "Deblurring and sparse unmixing for hyperspectral images," *IEEE Transactions on Geoscience and Remote Sensing*, vol. 51, pp. 4045–4058, 2013.
[42] L. Miao, H. Qi, and H. Szu, "A maximum entropy approach to unsupervised mixed-pixel decomposition," *IEEE Transactions on Image Processing*, vol. 16, no. 4, pp. 1008–1021, 2007.
[43] R. Chan, S. Riemenschneider, L. Shen, and Z. Shen, "Tight frame: an efficient way for high-resolution image reconstruction," *Applied Computational Harmonic Analysis*, vol. 17, pp. 91–115, 2004.
[44] J. Cai, R. Chan, and Z. Shen, "A framelet-based image inpainting algorithm," *Applied Computational Harmonic Analysis*, vol. 24, no. 2, pp. 131–149, 2008.
[45] J. Cai, H. Ji, C. Liu, and Z. Shen, "Framelet-based blind motion deblurring from a single image," *IEEE Transactions on Image Processing*, vol. 21, no. 2, pp. 562–572, 2012.
[46] B. Dong and Z. Shen, "MRA based wavelet frames and applications," *IAS Lecture Notes Series, Summer Program on The Mathematics of Image Processing, Park City Mathematics Institute*, 2010.
[47] A. Ron and Z. Shen, "Affine systems in $l_2(\mathbb{R}^d)$: The analysis of the analysis operator," *Journal of Functional Analysis*, vol. 148, no. 2, pp. 408–447, 1997.
[48] A. Chai and Z. Shen, "Deconvolution: A wavelet frame approach," *Numerische Mathematik*, vol. 106, no. 4, pp. 529–587, 2007.
[49] X. Tai and C. Wu, "Augmented lagrangian method, dual methods and split bregman iteration for ROF model," in *Scale Space and Variational Methods in Computer Vision*, 2009, pp. 502–513.
[50] T. Goldstein and S. Osher, "The split bregman method for l1-regularized problems," *SIAM Journal on Imaging Sciences*, vol. 2, no. 2, pp. 323–343, 2009.
[51] E. Esser, "Primal dual algorithms for convex models and applications to image restoration, registration and nonlocal inpainting," Ph.D. dissertation, University of California Los Angeles, 2010.
[52] A. Chambolle, "An algorithm for total variation minimization and applications," *Journal of Mathematical Imaging and Vision*, vol. 20, no. 1, pp. 89–97, 2004.
[53] D. L. Donoho, "De-noising by soft-thresholding," *IEEE Transactions on Information Theory*, vol. 41, no. 3, pp. 613–627, 1995.
[54] J. Cai, S. Osher, and Z. Shen, "Split bregman methods and frame based image restoration," *Multiscale Modeling & Simulation*, vol. 8, no. 2, pp. 337–369, 2009.
[55] M. Iordache, J. Bioucas-Dias, and A. Plaza, "Total variation regulatization in sparse hyperspectral unmixing," in *3rd Workshop on Hyperspectral Image and Signal Processing: Evolution in Remote Sensing (WHISPERS)*, 2011, pp. 1–4.
[56] J. Plaza, A. Plaza, P. Martínez, and R. Pérez, "H-comp: A tool for quantitative and comparative analysis of endmember identification algorithms," in *IEEE International Geoscience and Remote Sensing Symposium, IGARSS'03. Proceedings.*, vol. 1, 2003, pp. 291–293.

Guixu Zhang received the Ph.D. degree from Institute of Modern Physics, Chinese Academy of Sciences, Lanzhou, China, in 1998. He is currently a Professor in Department of Computer Science and Technology, East China Normal University, Shanghai, China. His research interests include hyperspectral remote sensing, image processing, and artificial intelligence.

Yingying Xu received the B.Sc. degree in Computer Science from Zhejiang Gongshang University, Hangzhou, China, in 2013. She is currently a Ph.D. student with the Department of Computer Science, East China Normal University, Shanghai, China. Her main research area is image processing using mathematical methods.

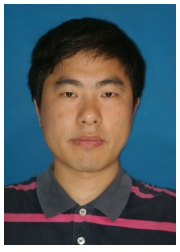

Faming Fang received the Ph.D. degree in Computer Science from East China Normal University, Shanghai, China, in 2013. He is currently a Lecturer with the Department of Computer Science, East China Normal University, Shanghai, China. His main research area is image processing using the variational methods and PDEs.